OPEN ACCESS
JOURNAL OF ADVANCED DIELECTRICS
Vol. 11, No. 5 (2021) 2160003 (9 pages)

DOI: 10.1142/S2010135X21600031

Comparative study on the performance of piezo-active 1–3-type composites with lead-free components

Ashura N. Isaeva and Vitaly Yu. Topolov*
Department of Physics, Southern Federal University
5 Zorge Street, 344090 Rostov-on-Don, Russia
*vutopolov@sfedu.ru

Received 19 April 2021; Accepted 21 May 2021; Published 23 June 2021

Piezoelectric properties and related figures of merit are studied in novel 1–3-type composites based on ferroelectric domain-engineered lead-free single crystal with the relatively large longitudinal piezoelectric coefficient d_{33}. Relationships between the piezoelectric properties and the set of figures of merit are analyzed for the 1–3 and 1–3–0 composites that contain the same single-crystal and polymer components. For a composite characterized by 1–3–0 connectivity, an influence of a porous piezo-passive matrix on the figures of merit and their volume-fraction behavior is considered additionally. A large anisotropy of figures of merit is observed in the 1–3–0 composite with specific porous matrices. A diagram is put forward to show volume-fraction regions of the large anisotropy of figures of merit of the studied 1–3–0 composite. Due to large figures of merit and their considerable anisotropy, the studied lead-free composites can be applied in piezoelectric energy-harvesting systems, sensors, transducers, and so on.

Keywords: Lead-free composite; figures of merit; piezoelectric properties; 1–3 connectivity; 1–3–0 connectivity.

1. Introduction

There has been significant interest in piezoelectric energy harvesting[1–4] concerned with the successful development of low-powered electronics, wireless sensor technologies and related applications.[5–11] In a general case, energy harvesting is a physical process of capturing, accumulating, and storing portions of energy from external sources.[1–3] Among modern high-performance piezoelectric materials to be of importance in this field of research and applications, we mention composites that are based on lead-free ferroelectric single crystals (SCs) split into non-180° domains. As follows from literature data, these composites are mainly of the 1–3-type[3,6,12,13] and 2–2-type.[3,14,15] The α–β connectivity is written in the form put forward by Newnham *et al*.[16]

To the best of our knowledge, despite the known effective electromechanical properties of some lead-free composites,[12,15,17] the system of their figures of merit (FOMs) was not yet studied in detail. The study on FOMs is topical because the modified FOMs[18] concerned with the piezoelectric effect are useful for a more careful characterization of materials at the energy conversion and harvesting under mechanical loading. Relationships between the piezoelectric properties and traditional (also often termed "energy-harvesting") FOMs of the composite[3,18] are taken into consideration at the interpretation of its performance.[6] The aim of the present paper is to describe the piezoelectric coefficients and related FOMs of the lead-free 1–3 and 1–3–0 composites in a wide volume-fraction range.

2. Model and Effective Properties of the Composite

In Sec. 2, we describe our model concept and procedure to evaluate the effective electromechanical properties and FOMs of the 1–3-type composites based on lead-free domain-engineered SCs.

2.1. *Model concept related to 1–3 and 1–3–0 connectivity patterns*

The composite shown in Fig. 1 is characterized as a system of long ferroelectric SC rods in a large polymer matrix. Each SC rod is parallelepiped-shaped and having a square base that is parallel to the co-ordinate OX_3 axis. The spontaneous polarization of each SC rod is $\boldsymbol{P}_s^{(1)} \uparrow\uparrow OX_3$, and OX_3 is the poling axis of the composite sample. The typical domain arrangement in the rod is shown in inset 1 in Fig. 1. Centers of the rod bases form a simple square lattice in the (X_1OX_2) plane, and lattice unit-cell vectors are parallel to the OX_k axes shown in Fig. 1. The crystallographic axes $X^{(1)}$, $Y^{(1)}$, and $Z^{(1)}$ of each SC rod obey conditions $X^{(1)} \parallel OX_1$, $Y^{(1)} \parallel OX_2$, and $Z^{(1)} \parallel OX_3$.

*Corresponding author.

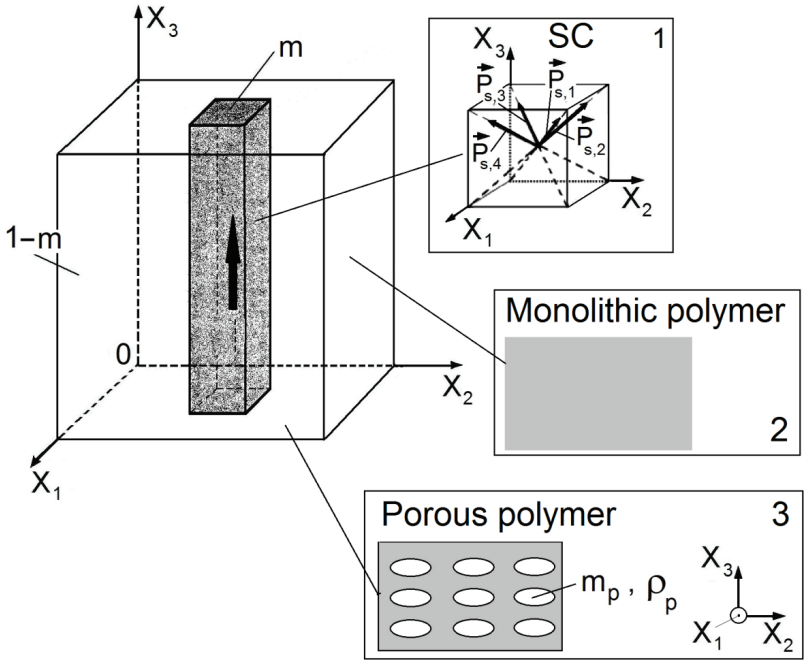

Fig. 1. Schematic diagram of the 1–3-type composite, arrangement of non-180° domains in the SC rod (inset 1) and fragments of the polymer matrix (insets 2 and 3). ($X_1X_2X_3$) is a Cartesian co-ordinate system, m and $1-m$ are volume fractions of SC and polymer, respectively. The arrow shows the poling direction in the SC rod and composite sample as a whole. In inset 1, the schematic arrangement of non-180° domains in the SC rod poled along the (OX_3) axis is shown. In inset 3, m_p is porosity of the polymer matrix, and ρ_p is the aspect ratio of the pore therein.

The matrix surrounding the rods can be either monolithic or porous as shown in insets 2 and 3 in Fig. 1.

The composite with the monolithic matrix (Fig. 1) is characterised by 1–3 connectivity, and the composite with the porous matrix is characterized by 1–3–0 connectivity, where the polymer matrix with isolated air pores is described by 3–0 connectivity (see inset 3 in Fig. 1). Each pore of the polymer matrix is described in the co-ordinate ($X_1X_2X_3$) system by the equation

$$(x_1/a_{p1})^2 + (x_2/a_{p2})^2 + (x_3/a_{p3})^2 = 1. \quad (1)$$

In Eq. (1) $a_{p1} = a_{p2}$ and a_{p3} are semi-axes of the air pore. Hereafter, we describe the porous matrix in terms of the volume fraction of pores m_p in the polymer matrix (i.e., porosity of the matrix) and the aspect ratio of the pore $\rho_p = a_{p1}/a_{p3}$. Centers of these pores form a simple tetragonal lattice which unit-cell vectors are parallel to OX_k. It is assumed that the pore semi-axes a_{p1} and a_{p3} from Eq. (1) are much smaller than the length of the base side of the SC rod. In this case, we can consider the porous polymer medium as an effective medium which properties are to be determined before the avergaing procedure[3,6] for the 1–3 composite structure.

2.2. *Effective electromechanical properties and parameters of studied composites*

Effective electromechanical properties of the 1–3–0 composite with the porous matrix (see inset 3 in Fig. 1) are found in two stages. In the first stage, the effective properties of the porous matrix are determined in terms of work[19] (dilute approach) and given by

$$\|\boldsymbol{C}^{(2)}\| = \|\boldsymbol{C}^{(p)}\| \cdot [\|\boldsymbol{I}\| - m_p (\|\boldsymbol{I}\| - (1 - m_p) \|\boldsymbol{S}\|)^{-1}]. \quad (2)$$

In Eq. (2), $\|\boldsymbol{C}^{(p)}\|$ is the 9×9 matrix that describes the properties of monolithic polymer, $\|\boldsymbol{I}\|$ is the 9×9 identity matrix, and $\|\boldsymbol{S}\|$ is the 9×9 matrix that contains components of the electroelastic Eshelby tensor.[20] This tensor is used to take into consideration boundary conditions for electric and elastic fields[19,20] in the spheroidal pore and surrounding polymer medium, as well as to describe a concentration of the electric and mechanical fields in the pore. The $\|\boldsymbol{S}\|$ elements depend[20] on the aspect ratio ρ_p and properties of polymer, i.e., on elements of $\|\boldsymbol{C}^{(p)}\|$ from Eq. (2). The latter matrix can be written as follows:

$$\left\|\boldsymbol{C}^{(p)}\right\| = \begin{pmatrix} \left\|c^{(p),E}\right\| & \left\|e^{(p)}\right\|^t \\ \left\|e^{(p)}\right\| & -\left\|\varepsilon^{(p),\xi}\right\| \end{pmatrix}. \quad (3)$$

In Eq. (3), $\|\boldsymbol{c}^{(p),E}\|$ is the 6×6 matrix of elastic moduli of polymer at external electric field $E = \text{const}$, $\|\boldsymbol{e}^{(p)}\|$ is the 6×3 matrix of piezoelectric coefficients of polymer, $\|\boldsymbol{e}^{(p),\xi}\|$ is the 3×3 matrix of its dielectric permittivities measured at mechanical strain $\xi = \text{const}$, and "t" is introduced to denote the matrix transposition. The $\|\boldsymbol{C}^{(2)}\|$ matrix from Eq. (2) has the form shown in Eq. (3).

The second stage means evaluations of the effective electromechanical properties of the 1–3-type composite (Fig. 1). Hereby, we apply the matrix method.[3,6,17,21] Based on this method, we write the matrix of the effective properties of the composite $\| \boldsymbol{C}^* \|$ in the following form:

$$\| \boldsymbol{C}^* \| = [\| \boldsymbol{K}^{(1)} \| \cdot \| \boldsymbol{M} \| m^+ \| \boldsymbol{K}^{(2)} \| (1-m)] \cdot [\| \boldsymbol{M} \| m^+ \| \boldsymbol{I} \| (1-m)]^{-1}. \quad (4)$$

The $\| \boldsymbol{K}^{(1)} \|$ matrix from Eq. (4) describes the properties of the SC rod, $\| \boldsymbol{K}^{(2)} \|$ is used to describe the properties of the composite matrix that surrounds the SC rods, and $\| \boldsymbol{M} \|$ is related to the boundary conditions[3] at the planar vertical boundaries in the composite (see Fig. 1). It is assumed that the mechanical stress and electric fields in each SC rod are uniform, and the boundary between the rod and surrounding matrix of the composite sample is infinitely thin. The $\| \boldsymbol{C}^* \|$ matrix from Eq. (4) is written in the general form as

$$\left\| \boldsymbol{C}^* \right\| = \begin{pmatrix} \left\| s^{*E} \right\| & \left\| d^* \right\|^t \\ \left\| d^* \right\| & \left\| \varepsilon^{*\sigma} \right\| \end{pmatrix}. \quad (5)$$

In Eq. (5), $\| \boldsymbol{s}^{*E} \|$ is the 6×6 matrix of elastic compliances of the composite at $E = \text{const}$, $\| \boldsymbol{d}^* \|$ is the 6×3 matrix of piezoelectric coefficients, and $\| \boldsymbol{e}^{*\sigma} \|$ is the 3×3 matrix of dielectric permittivities of the composite at mechanical stress $\sigma = \text{const}$. By analogy with Eq. (3), we use the superscript "t" in Eq. (5) to denote the matrix transposition.

The $\| \boldsymbol{K}^{(1)} \|$ and $\| \boldsymbol{K}^{(2)} \|$ matrices from Eq. (4) have the form that is similar to that shown in Eq. (5). The $\| \boldsymbol{K}^{(2)} \|$ matrix related to the monolithic polymer matrix in the 1–3 composite is to be written directly, without taking into account the first stage of evaluations. A transition from $\| \boldsymbol{C}^{(2)} \|$ in Eq. (2) ($\| \boldsymbol{C}^{(2)} \|$ characterizes the porous polymer matrix, as described in the first stage) to $\| \boldsymbol{K}^{(2)} \|$ in Eq. (5) is performed by using conventional formulae[22] for a piezoelectric medium. It should be noted that the $\| \boldsymbol{C}^* \|$ matrix from Eqs. (4) and (5) depends on the volume fraction of SC m (in the case of the 1–3 composite) or on m, porosity m_p and aspect ratio of the pore ρ_p (for the 1–3–0 composite), see Fig. 1. Elements of $\| \boldsymbol{C}^* \|$ from Eq. (4) are evaluated within the framework of the so-called long-wave approximation.[3,6] According to this approximation, a wavelength of an external field acting on the composite sample (Fig. 1) is assumed to be much longer than the length of the SC rod (in the 1–3 composite) or much longer than the largest axis of the pore in the matrix of the 1–3–0 composite.

Knowing the $\| \boldsymbol{C}^* \|$ elements from Eq. (4), one can evaluate the following effective parameters of the composite in the wide volume-fraction (m) range:

(i) piezoelectric coefficients d_{3j}^* and g_{3j}^*,
(ii) traditional (energy-harvesting or squared) FOMs[3,6,18]

$$(Q_{3j}^*)^2 = d_{3j}^* g_{3j}^*, \quad (6)$$

(iii) the transmission coefficient,[18] i.e., the maximum "output electrical energy/input mechanical energy" ratio

$$\lambda_{3j,m}^* = [(k_{3j}^*)^{-1} - ((k_{3j}^*)^{-2} - 1)^{1/2}]^2, \quad (7)$$

(iv) the "maximum output electrical energy/stored electrical energy" ratio[18,23]

$$L_{3j}^* = \lambda_{3j,m}^* / (k_{3j}^*)^2, \quad (8)$$

(v) FOM for a stress-driven piezoelectric energy harvester[18]

$$F_{3j}^{*\sigma} = L_{3j}^* (Q_{3j}^*)^2, \quad (9)$$

and

(vi) FOM for a strain-driven piezoelectric energy harvester[18]

$$F_{3j}^{*\xi} = F_{3j}^{*\sigma} / (s_{jj}^{*E} s_{jj}^{*D}), \quad (10)$$

where $j = 1$, 2, and 3. A relation between the piezoelectric coefficients involved in Eq. (6) is expressed[22] by

$$d_{3j}^* = \varepsilon_{3j}^{*\sigma} g_{fj}^*. \quad (11)$$

In Eqs. (7) and (8),

$$k_{ij}^* = d_{ij}^* / (\varepsilon_{ii}^{*\sigma} s_{jj}^{*E})^{1/2} \quad (12)$$

is the electromechanical coupling factor. This physical parameter describes[1–3,6] an effectiveness of an energy conversion from the mechanical form into the electrical form and vice versa. FOMs $(Q_{3j}^*)^2$ from Eq. (6) at $j = 1$, 2, and 3 enable one to estimate the "signal/noise' ratio of piezoelectric material.[3] Electromechanical coupling factors k_{31}^* and k_{32}^* from Eq. (12) are taken as absolute values in Eq. (7). In Eq. (10), $s_{jj}^{*\mathrm{D}}$ is the elastic compliance at electric displacement $D = \text{const}$.

The effective properties and FOMs of the composites are evaluated by using experimental data on the ferroelectric domain-engineered SC and polymer components. The perovskite-type $[\mathrm{Li}_x(\mathrm{K}_{1-y}\mathrm{Na}_y)_{1-x}](\mathrm{Nb}_{1-z}\mathrm{Ta}_z)\mathrm{O}_3$:Mn (KNNTL-Mn) SC[24] poled along [001] (i.e., parallel to OX_3, see inset 1 of Fig. 1) is the only piezoelectric component of the studied composites, where molar concentrations are $x = 0.06$, $y = 0.1$–0.3, $z = 0.07$–0.17, and the level of Mn doping is 0.25 mol%. In Table 1, we show the full set of room-temperature electromechanical constants of this poled SC. In Table 2, we list constants of polyurethane[25] and araldite[21] which are used to form the composite matrices. The [001]-poled KNNTL-Mn SC is of great interest[24] due to its relatively large piezoelectric coefficient $d_{33} = 545$ pC/N and very large piezoelectric coefficient $g_{33} = 94.7$ mV·m/N. In this context, we underline

Table 1. Elastic compliances s_{ab}^E (in 10^{-12} Pa^{-1}), piezoelectric coefficients d_{ij} (in pC/N) and dielectric permittivity $\varepsilon_{pp}^{\sigma}$ of the [001]-poled domain-engineered KNNTL-Mn SC with 4*mm* symmetry.[24]

s_{11}^E	s_{12}^E	s_{13}^E	s_{33}^E	s_{44}^E	s_{66}^E	d_{31}	d_{33}	d_{15}	$\varepsilon_{11}^{\sigma}/\varepsilon_0$	$\varepsilon_{33}^{\sigma}/\varepsilon_0$
33.4	–7.36	–25.8	57.7	12.8	13.5	–260	545	66	400	650

Table 2. Elastic moduli c_{ab} (in 10^{10} Pa), elastic compliances s_{ab} (in 10^{-12} Pa^{-1}) and dielectric permittivity ε_{pp} of polymers.

Polymers	c_{11}	c_{12}	s_{11}	s_{12}	$\varepsilon_{pp}/\varepsilon_0$
Araldite[21]	0.78	0.44	216	−78	4.0
Polyurethane[25]	0.442	0.260	405	−151	3.5

that the aforementioned d_{33} and g_{33} values of KNNTL-Mn are larger than the similar parameters of widespread poled ceramics[3] based on Pb(Zr, Ti)O_3.

3. Piezoelectric Performance and FOMs

Some volume-fraction (m and m_p) dependence of FOMs from Eqs. (6)–(10) are analyzed in Sec. 3. Below we consider specifics of FOMs of the lead-free 1–3 and 1–3–0 composites which structure is shown in Fig. 1.

3.1. *Parameters of 1–3 composites*

Figures 2 and 3 illustrate specifics of the volume-fraction behavior of the piezoelectric response and FOMs that are related to the longitudinal ($j = 3$) and transverse ($j = 1$) piezoelectric effect. The system of the parallel poled ferroelectric SC rods in the 1–3 composite (Fig. 1) promotes a relatively rapid increase and further saturation of the piezoelectric coefficient $d_{33}^*(m)$ [curve 1 in Figs. 2(a) and 3(a)]. On increasing the volume fraction m, the piezoelectric coefficient $d_{31}^*(m)$ decreases more slowly in comparison to $d_{33}^*(m)$, and no saturation of the $d_{31}^*(m)$ curve is observed in the whole m range [see curve 2 in Figs. 2(a) and 3(a)]. Replacing the araldite matrix with the softer polyurethane matrix in the composite enables us to observe the saturation of the $d_{33}^*(m)$ curve at smaller m values, compare curve 1 in Fig. 3(a) to curve 1 in Fig. 2(a). The piezoelectric coefficient $g_{33}^*(m)$ of the polyurethane-containing composite has the larger and sharper maximum, as follows from comparison of curve 3 in Fig. 3(a)

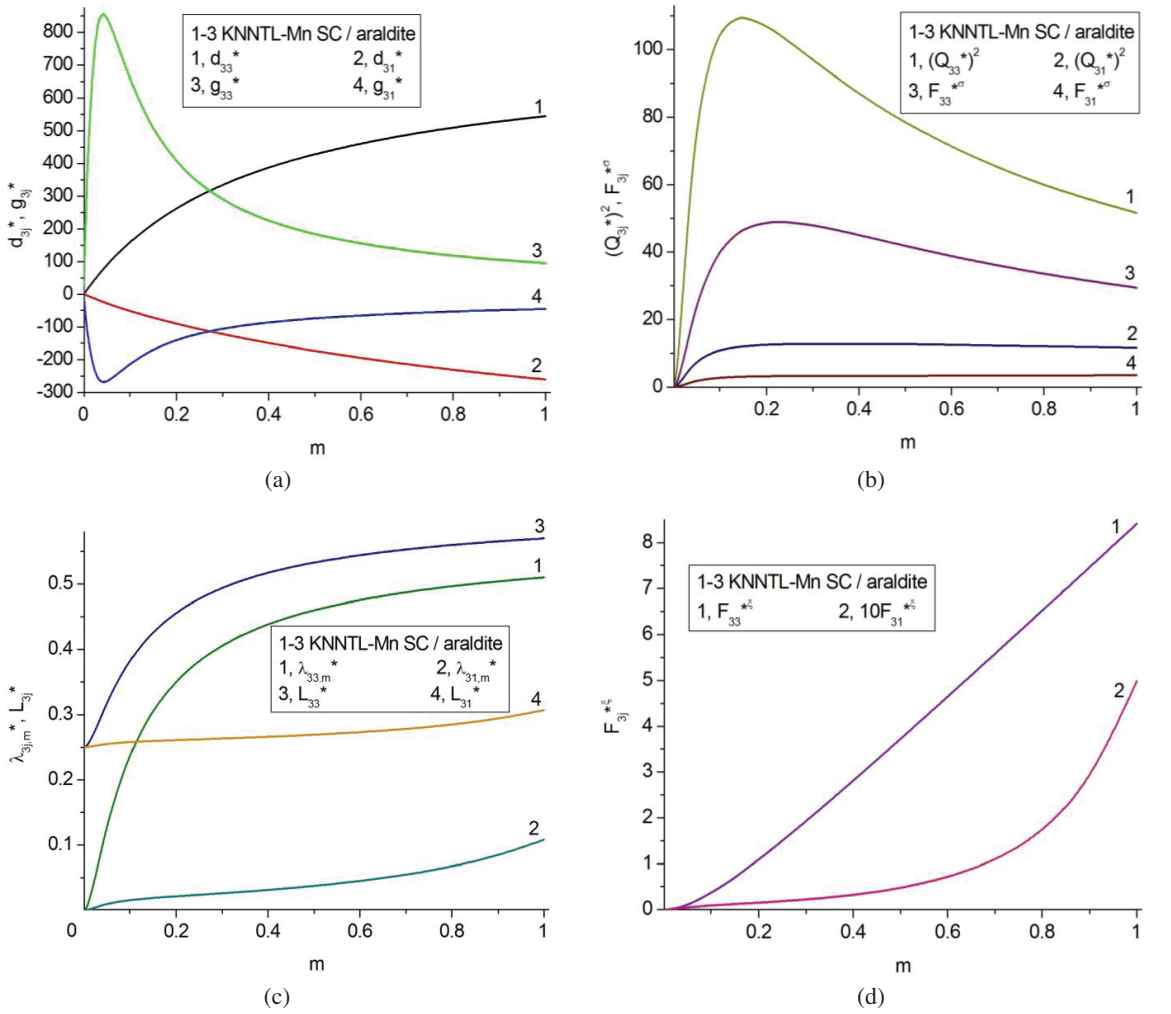

Fig. 2. Piezoelectric coefficients d_{3j}^* (a, in pC/N) and g_{3j}^* (a, in mV·m/N), and FOMs $(Q_{3j}^*)^2$ and $F_{3j}^{*\sigma}$ (b, in 10^{-12} Pa^{-1}), $\lambda_{3j,m}^*$ and L_{3j}^* (c), and $F_{3j}^{*\xi}$ (d, in 10^{10} Pa) of the 1–3 KNNTL-Mn SC/araldite composite.

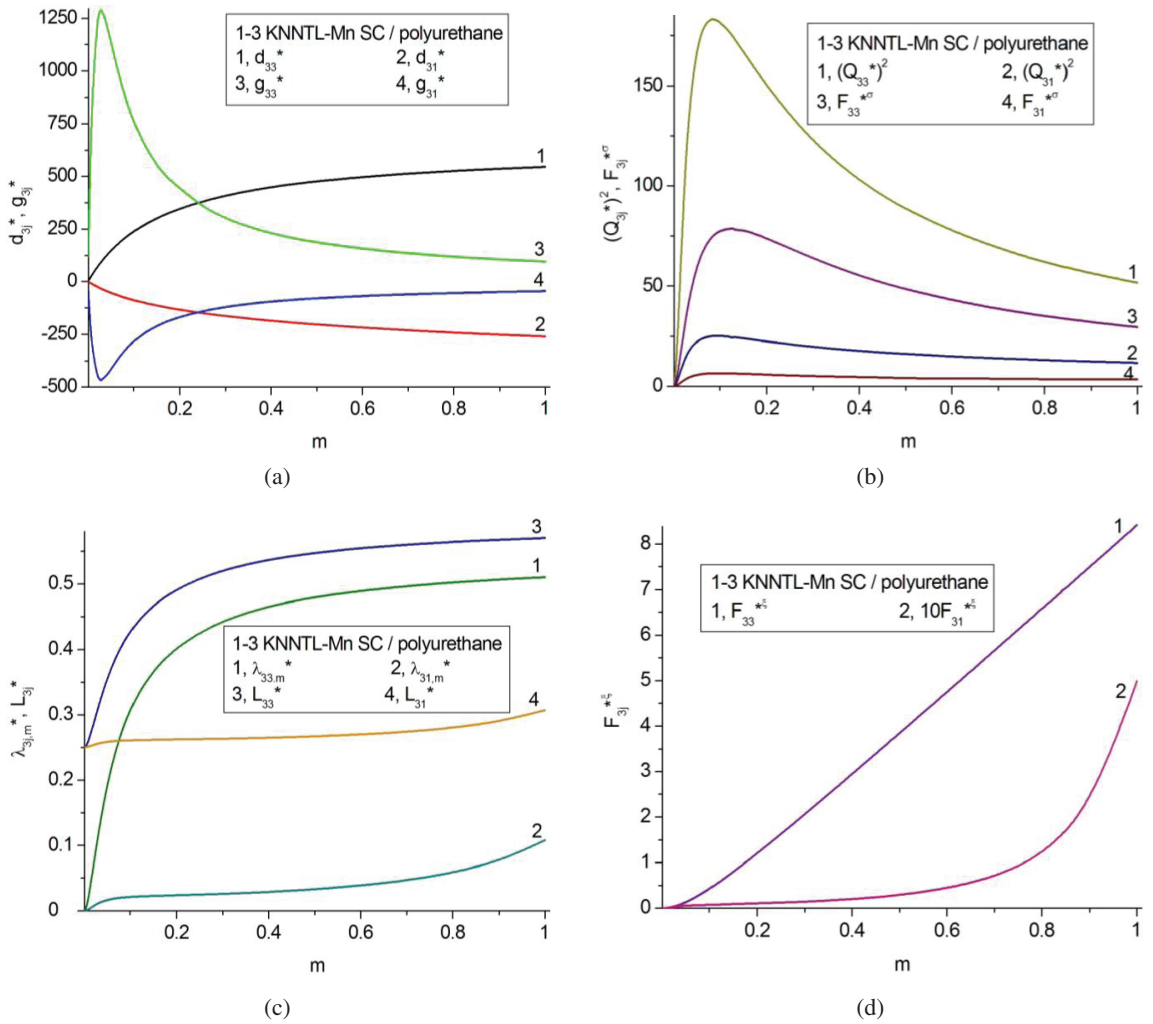

Fig. 3. Piezoelectric coefficients d_{3j}^* (a, in pC/N) and g_{3j}^* (a, in mV·m/N), and FOMs $(Q_{3j}^*)^2$ and $F_{3j}^{*\sigma}$ (b, in 10^{-12} Pa^{-1}), $\lambda_{3j,m}^*$ and L_{3j}^* (c), and $F_{3j}^{*\xi}$ (d, in 10^{10} Pa) of the 1–3 KNNTL-Mn SC/polyurethane composite.

to curve 3 in Fig. 2(a). The relation between d_{3j}^* and g_{3j}^* in accordance with Eq. (11) explains the presence of max g_{33}^* and min g_{31}^* [see curves 3 and 4 in Figs. 2(a) and 3(a)] at $m << 1$. This is the volume-fraction range where the dielectric permittivity $\varepsilon_{33}^{*\sigma}$ of the composite is comparable to $\varepsilon_{33}^{(p)}$ of its polymer component. It is noteworthy that max g_{33}^* and min g_{31}^* of the 1–3 are observed at the almost equal volume fractions m [cf. curves 3 and 4 in Fig. 2(a)], and these m values decrease in a case of the softer matrix surrounding the rods.

The aforementioned nonmonotonic $g_{3j}^*(m)$ dependences influence the volume-fraction behavior of $(Q_{3j}^*)^2$ and $F_{3j}^{*\sigma}$ to a large degree [Figs. 2(b) and 3(b)]. It is seen that, by analogy with max g_{33}^*, the larger max$[(Q_{33}^*)^2]$ and max $F_{33}^{*\sigma}$ values [see Fig. 3(b)] are achieved in the presence of the softer (i.e., polyurethane) matrix of the 1–3 composite. An analogy between the nonmonotonic $[(Q_{33}^*(m)]^2$ and $F_{33}^{*\sigma}(m)$ dependences [compare curves 1 and 3 in Fig. 3, a or curves 1 and 3 in Fig. 3(b)] is accounted for their relation according to Eq. (9) and for the nonmonotonic $L_{33}^*(m)$ dependence [curve 3 in Figs. 2(c) and 3(c)]. Both the $L_{3j}^*(m)$ and $\lambda_{3j,m}^*(m)$ dependences that are related by Eq. (8) show monotonic increasing, see Figs. 2(c) and 3(c). The similar configuration of the $L_{33}^*(m)$ and $\lambda_{33,m}^*(m)$ curves [see curves 1 and 3 in Figs. 2(c) and 3(c)] is caused by the electromechanical coupling factor k_{33}^* involved in Eqs. (7) and (8). According to Eq. (12), $k_{33}^* \sim d_{33}^*$, and the piezoelectric coefficient d_{33}^* exhibits the monotonic behavior [see curve 1 in Figs. 2(a) and 3(a)]. The minor changes in the $L_{31}^*(m)$ and $\lambda_{31,m}^*(m)$ curves [see curves 2 and 4 in Figs. 2(c) and 3(c)] can be accounted for by the less pronounced transverse piezoelectric effect in the composite sample with the piezo-passive matrix. FOMs $F_{3j}^{*\xi}(m)$ from Eq. (11) are characterized by the monotonic volume-fraction dependence and minor changes [Figs. 2(d) and 3(d)] on replacing the polymer matrix in the 1–3 composite. The presence of the $s_{jj}^{*E} s_{jj}^{*D}$ denominator in Eq. (12) leads to the monotonic $F_{3j}^{*\xi}(m)$ dependence in contrast to the

nonmonotonic $F_{3j}^{*\sigma}(m)$ dependence related to the same composite. Curve 1 in Figs. 2(d) and 3(d) suggests that $F_{33}^{*\xi}(m)$ increases more rapidly in comparison to $F_{31}^{*\xi}(m)$, and this can be concerned with specifics of the transverse piezoelectric effect in the composite. The large difference between the elastic properties of the anisotropic SC and isotropic polymer from Tables 1 and 2 promotes a large difference between $F_{33}^{*\xi}(m)$ and $F_{31}^{*\xi}(m)$ in the whole m range [see Figs. 2(d) and 3(d)]. It should be added that FOMs $F_{3j}^{*\xi}$ exhibit the most significant anisotropy among the studied FOMs from Eqs. (6)–(10).

3.2. *Parameters of 1–3–0 composites*

The porous structure in the polymer matrix (see inset 3 in Fig. 1) leads to changes in its elastic properties that influence FOMs of the 1–3–0 composite as compared to its 1–3 analog. Now we consider the volume-fraction (m) behavior of FOMs of the 1–3–0 composite (Fig. 4) at some fixed values of the aspect ratio ρ_p and porosity m_p of the composite matrix. Polyurethane is the softer polymer component among those listed in Table 2. Hereafter we vary the aspect ratio ρ_p of the pore from 1 (spherical pore) to 100 (heavily oblate pore).

Volume-fraction (m) dependences of FOMs L_{3j}^{*}, $\lambda_{3j,m}^{*}$ and $F_{3j}^{*\xi}$ undergo minor changes at aspect ratios from the range of $1 \le \rho_p \le 100$ and at porosity m_p from 0.2 to 0.3. We show typical examples of these dependences in Figs. 4(a) and 4(b). Most important changes in the volume-fraction dependences are related to FOMs $(Q_{3j}^{*})^2$ and $F_{3j}^{*\sigma}$. As in the case of the 1–3 composite [see Figs. 2(b) and 2(b)], we observe the consistent nonmonotonic behavior of $(Q_{3j}^{*})^2$ and $F_{3j}^{*\sigma}$ [see Figs. 4(c)–4(f). Increasing ρ_p at m_p = const in the polymer matrix leads to increasing max $[(Q_{3j}^{*})^2]$ and max $F_{3j}^{*\sigma}$ [see curves 1 and 3 in Figs. 4(c)–4(e)] due to the larger max g_{33}^{*} value. The larger max g_{33}^{*} value is observed at a smaller volume fraction of SC m and caused by the active influence of the porous polymer matrix with a smaller dielectric permittivity $\varepsilon_{33}^{(2)}$. In this case, there is shifting max $[(Q_{3j}^{*})^2]$ and

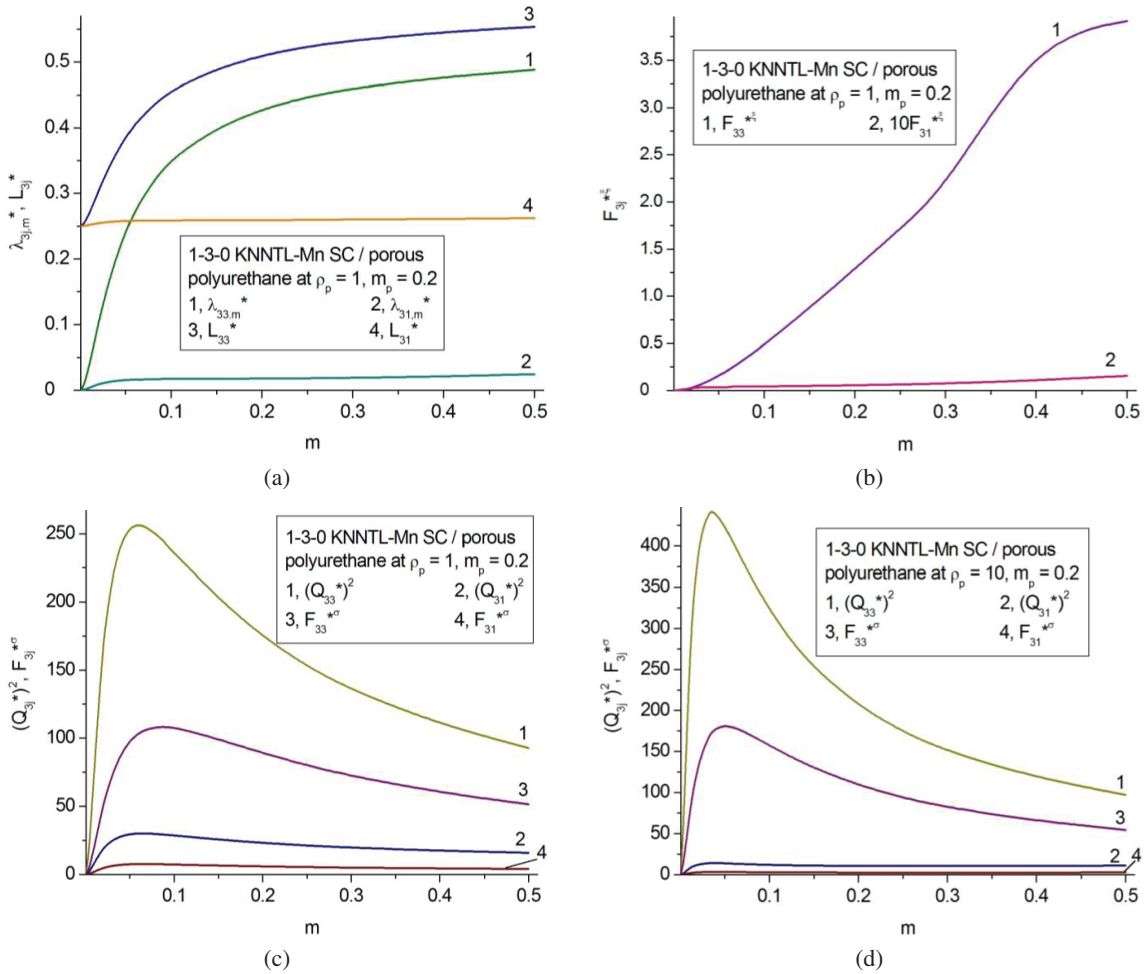

Fig. 4. FOMs $\lambda_{3j,m}^{*}$ and L_{3j}^{*} (a), $F_{3j}^{*\xi}$ (b, in 10^{10} Pa), and $(Q_{3j}^{*})^2$ and $F_{3j}^{*\sigma}$ (c–f, in 10^{-12} Pa^{-1}) of the 1–3–0 KNNTL-Mn SC/porous polyurethane composite at ρ_p = const and m_p = const.

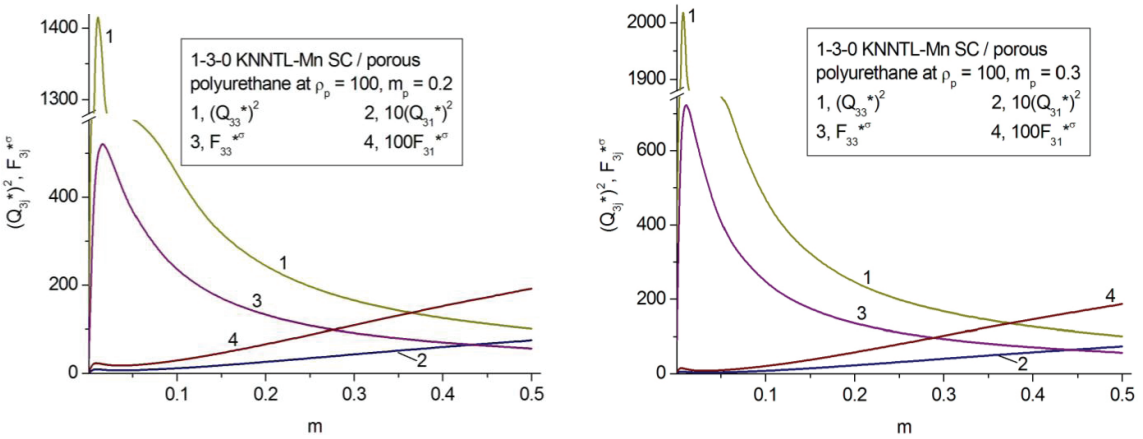

(e) (f)

Fig. 4. (*Continued*)

max $F_{3j}^{*\sigma}$ locations towards the smaller volume fractions m [cf. Figs. 4(c) and 4(e)]. Graphs in Figs. 4(c)–4(e) enable us to conclude that increasing ρ_p at m_p = const promotes the large anisotropy of FOMs $(Q_{3j}^*)^2$ and $F_{3j}^{*\sigma}$ because of the considerable weakening of the transverse piezoelectric effect in the composite with the polymer matrix that contains the heavily oblate pores ($\rho_p >> 1$). Increasing porosity m_p at ρ_p = const also leads to increasing max $[(Q_{3j}^*)^2]$ and max $F_{3j}^{*\sigma}$, and these maxima shift towards the smaller volume fractions of SC m [cf. Figs. 4(e) and 4(f)]. Additionally, increasing m_p in the polymer matrix promotes the large anisotropy of both $(Q_{3j}^*)^2$ and $F_{3j}^{*\sigma}$.

$$(Q_{33}^*)^2/(Q_{31}^*)^2 \geq 100, \quad \lambda_{33,m}^*/\lambda_{31,m}^* \geq 100, \quad F_{33}^{*\sigma}/F_{31}^{*\sigma} \geq 100, \quad \text{and} \quad F_{33}^{*\xi}/F_{31}^{*\xi} \geq 100 \tag{13}$$

Our analysis of the volume-fraction (m) behavior of FOMs from Eqs. (6)–(10) enables us to conclude that the 1–3–0 composite exhibits a large anisotropy of four types of FOMs. Four conditions for the large anisotropy hold, and we show the respective regions with arrows 1–4 at the diagram (Fig. 5). From Fig. 5, m ranges related to validity of conditions (13) become wider on increasing porosity m_p. The very large $(Q_{33}^*)^2/(Q_{31}^*)^2$, $\lambda_{33,m}^*/\lambda_{31,m}^*$ and $F_{33}^{*\sigma}/F_{31}^{*\sigma}$ ratios are achieved at $m < 0.5$ (see arrows 1–3 in Fig. 5), i.e., in a region of the active influence of the porous matrix on the piezoelectric performance and FOMs of the 1–3–0 composite. Its porous polymer matrix at $\rho_p >> 1$ exhibits the large anisotropy of its elastic compliances, e.g., the condition $s_{33}^{(2)} >> s_{11}^{(2)}$ holds in a specific porosity (m_p) range. Such an elastic anisotropy strongly influences the piezoelectric performance, related FOMs and anisotropy of the 1–3–0 composite.

The studied piezo-active composites exhibit some advantages over the 1–3-type composites described in literature. A lead-free 1–3 SC-based composite at the volume fraction of SC $m \approx 0.52$ is characterized[12] by FOM $(Q_{33}^*)^2 = 23.7 \cdot 10^{-12}$ Pa^{-1}. As follows from our results, for the studied 1–3 composites

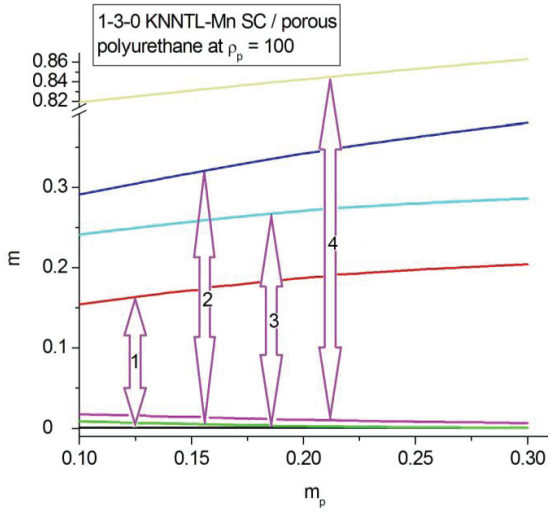

Fig. 5. Diagram that shows the volume-fraction (m and m_p) regions wherein conditions (13) hold for the 1–3–0 composite. Arrows 1, 2, 3, and 4 are related to regions where conditions $(Q_{33}^*)^2/(Q_{31}^*)^2 \geq 100$, $\lambda_{33,m}^*/\lambda_{31,m}^* \geq 100$, $F_{33}^{*\sigma}/F_{31}^{*\sigma} \geq 100$, and $F_{33}^{*\xi}/F_{31}^{*\xi} \geq 100$ hold, respectively.

at $m = 0.50$–0.55, values of FOM $(Q_{33}^*)^2 \approx 80 \cdot 10^{-12}$ Pa^{-1} are achieved, see curve 1 in Figs. 2(b) and 3(b). On a 1–3 lead-free ceramic-composite,[26] the piezoelectric coefficient $d_{33}^* = 350$ pC/N is measured. The largest piezoelectric coefficient g_{33}^* of a quasi 1–3 lead-free composite sample[27] is 510 mV·m/N. For a quasi 1–3 lead-free composite,[27] the FOM value is $(Q_{33}^*)^2 \approx 18 \cdot 10^{-12}$ Pa^{-1}. A 1–3 composite based on the domain-engineered $0.67Pb(Mg_{1/3}Nb_{2/3})O_3$–$0.33PbTiO_3$ SC poled along the crystallographic direction [001] of the perovskite unit cell is characterized[28] by FOMs $(Q_{33}^*)^2 \approx (100–200) \cdot 10^{-12}$ Pa^{-1} and $F_{33}^{*s} \approx 100 \cdot 10^{-12}$ Pa^{-1} at $m = 0.05$–0.70. These $(Q_{33}^*)^2$ and $F_{33}^{*\sigma}$ values[28] are comparable

to the similar parameters shown in Figs. 4(c)–4(f). We add for comparison that the piezoelectric coefficient d_{33} of the [001]-poled $0.67Pb(Mg_{1/3}Nb_{2/3})O_3$–$0.33PbTiO_3$ SC[29] is ca. 5.2 times larger than d_{33} of the [001]-poled KNNTL-Mn SC from Table 1.

4. Conclusions

The present paper has been devoted to the comparative study on the effective parameters of the lead-free 1–3-type composites based on [001]-poled domain-engineered SC. These effective parameters are used to describe the piezoelectric performance (piezoelectric coefficients d_{3j}^* and g_{3j}^*) and energetic characteristics [FOMs from Eqs. (6)–(10)] of the studied composites. Of interest is the volume-fraction dependence of the system of modified FOMs as shown in Figs. 2(b)–2(d), 3(b)–3(d), and 4. Examples of large FOMs and their links to the effective piezoelectric properties are analyzed in the present paper. The formation of the porous structure in the polymer matrix of the 1–3–0 composite at the aspect ratio $\rho_p \geq 1$ and volume fraction m = const leads to the appreciable increase of FOMs $(Q_{3j}^*)^2$ and $F_{3j}^{*\sigma}$ [see Figs. 4(c)–4(f)] in comparison to those of the 1–3 composite [see Fig. 3(b)]. The new diagram has been first built (see Fig. 5) to show the volume-fraction (m and m_p) regions where four conditions (13) for the large anisotropy of FOMs of the composite hold. This example of validity of conditions (13) is related to the 1–3–0 composite with the heavily oblate pores in its polymer matrix, i.e., at the aspect ratio of pores $\rho_p >> 1$.

Due to the system of large FOMs and their anisotropy, the studied lead-free 1–3-type composites are suitable as effective elements of modern piezoelectric sensors, transducers, and energy-harvesting systems wherein the longitudinal piezoelectric effect plays the leading role.

Acknowledgments

The authors are grateful to Prof. Dr. I. A. Parinov and Prof. Dr. A. E. Panich (Southern Federal University, Russia), and Prof. Dr. C. R. Bowen (University of Bath, UK) for their interest in the field of modern piezo-active materials and applications. Research was financially supported by Southern Federal University, grant No. VnGr-07/2020-04-IM (Ministry of Science and Higher Education of the Russian Federation).

References

[1]A. Erturk and D. J. Inman, *Piezoelectric Energy Harvesting* (Wiley, Chichester, 2011).
[2]S. Priya and D. J. Inman (eds.), *Energy Harvesting Technologies* (Springer, New York, 2009).
[3]C. R. Bowen, V. Yu. Topolov and H. A. Kim, *Modern Piezoelectric Energy-Harvesting Materials* (Springer International Publ. Switzerland, Cham, 2016).
[4]S. N. Shevtsov, A. N. Soloviev, I. A. Parinov, A. V. Cherpakov and V. A. Chebanenko, *Piezoelectric Actuators and Generators for Energy Harvesting. Research and Development* (Springer Nature, Cham, 2018).
[5]T. Hehn and Y. Manoli, *CMOS Circuits for Piezoelectric Energy Harvesters. Efficient Power Extraction, Interface Modeling and Loss Analysis* (Springer, Dordrecht, Heidelberg, New York, London, 2015).
[6]C. R. Bowen, V. Yu. Topolov, Y. Zhang and A. A. Panich, 1–3-type composites based on ferroelectrics: Electromechanical coupling, figures of merit, and piezotechnical energy-harvesting applications, *Energy Technol*. **6**, 813 (2018).
[7]R.-C. Wang, Y.-C. Lin, H.-C. Chen and W.-Y. Lin, Energy harvesting from g-C_3N_4 piezoelectric nanogenerators, *Nano Energy* **83**, 105743 (2020).
[8]H. Su, X. Wang, C. Li, Z. Wang, Y. Wu, J. Zhang, Y. Zhang, C. Zhao, J. Wu and H. Zheng, Enhanced energy harvesting ability of polydimethylsiloxane-$BaTiO_3$-based flexible piezoelectric nanogenerator for tactile imitation application, *Nano Energy* **83**, 105809 (2020).
[9]M. Sharma, A. Chauhan and R. Vaish, Energy harvesting using piezoelectric cementitious composites for water cleaning applications, *Mater. Res. Bull*. **137**, 111205 (2021).
[10]A. Wseem, M. AliJohar, M. Afifi Hassan, I. V. Bagal, J.-S. Ha, J. K. Lee and S.-W. Ryua, GaN/Al_2O_3 core-shell nanowire based flexible and stable piezoelectric energy harvester, *J. Alloys Compd*. **860**, 158545 (2021).
[11]S. Ge, Y. Xia, Y. Yang, J. Chen, Y. Peng, H. Xia, X. Wang and L. Qian, A sensorless self-tuning resonance system for piezoelectric broadband vibration energy harvesting, *IEEE Trans. Industr. Electronics* **68**, 2225–2235 (2021).
[12]D. Zhou, K. H. Lam, Y. Chen, Q. Zhang, Y. C. Chiu, H. Luo, J. Dai and H. L. W. Chan, Lead-free piezoelectric single crystal based 1–3 composites for ultrasonic transducer applications, *Sens. A. Actuators A* **182**, 95 (2012).
[13]K. Ren, Y. Liu, X. Geng, H. F. Hofmann and Q. M. Zhang, Single crystal PMN–PT/epoxy 1–3 composite for energy-harvesting application, *IEEE Trans. Ultrason., Ferroelectr., a. Freq. Control* **53**, 631 (2006).
[14]Z. Zeng, L. Gai, X. Wang, D. Lin, S. Wang, H. Luo and D. Wang, A plastic-composite-plastic structure high performance flexible energy harvester based on PIN-PMN-PT single crystal/epoxy 2–2 composite, *Appl. Phys. Lett*. **110**, 103501 (2017).
[15]V. Yu. Topolov and A. N. Isaeva, Hydrostatic piezoelectric parameters of lead-free 2–0–2 composites with two single-crystal components: Waterfall-like orientation dependences, *J. Adv. Dielect*. **10**, 2050015 (2020).
[16]R. E. Newnham, D. P. Skinner and L. E. Cross, Connectivity and piezoelectric – pyroelectric composites, *Mater. Res. Bull*. **13**, 525 (1978).
[17]V. Yu. Topolov, A. N. Isaeva and P. Bisegna, Novel lead-free composites with two porosity levels: Large piezoelectric anisotropy and high sensitivity, *J. Phys. D: Appl. Phys*. **53**, 395303 (2020).
[18]J. I. Roscow, H. Pearce, H. Khanbareh, S. Kar-Narayan and C. R. Bowen, Modified energy harvesting figures of merit for stress- and strain-driven piezoelectric systems, *Eur. Phys. J. Spec. Topics* **228**, 1537 (2019).
[19]M. L. Dunn and M. Taya, Electromechanical properties of porous piezoelectric ceramics, *J. Am. Ceram. Soc*. **76**, 1697 (1993).
[20]J. H. Huang and S. Yu, Electroelastic Eshelby tensors for an ellipsoidal piezoelectric inclusion, *Compos. Eng*. **4**, 1169 (1994).
[21]F. Levassort, M. Lethiecq, D. Certon and F. Patat, A matrix method for modeling electroelastic moduli of 0–3 piezo-composites, *IEEE Trans. Ultrason., Ferroelectr., a. Freq. Control* **44**, 445 (1997).
[22]T. Ikeda, *Fundamentals of Piezoelectricity* (Oxford University Press, Oxford, 1990).
[23]D. B. Deutz, J.-A. Pascoe, B. Schelen, S. van der Zwaag, D. M. de Leeuw and P. Groen, Analysis and experimental validation of the

figure of merit for piezoelectric energy harvesters, *Mater. Horiz*. **5**, 444 (2018).

[24]X. Huo, R. Zhang, L. Zheng, S. Zhang, R. Wang, J. Wang, S. Sang, B. Yang and W. Cao, (K, Na, Li)(Nb, Ta)O_3:Mn lead-free single crystal with high piezoelectric properties, *J. Am. Ceram. Soc*. **98**, 1829 (2015).

[25]L. V. Gibiansky and S. Torquato, On the use of homogenization theory to design optimal piezocomposites for hydrophone applications, *J. Mech. Phys. Soli*ds **45**, 689 (1997).

[26]Q. Ke, W.H. Liew, H. Tao, J. Wu, and K. Yao, KNNS-BNZH lead-free 1–3 piezoelectric composite for ultrasonic and photoacoustic imaging, *IEEE Trans. Ultrason., Ferroelec., A Freq. Contr.* **66**, 1395 (2019).

[27]V. L. Stuber, D. B. Deutz, J. Bennett, D. Cannel, D. M. de Leeuw, S. van der Zwaag and P. Groen, Flexible lead-free piezoelectric composite materials for energy harvesting applications, *Energy Technol.* **7**, 177 (2019).

[28]V. Yu. Topolov and A. N. Isaeva, Modified figures of merit of 1–3 composites based on ferroelectric crystals, *Zhurnal Tekhn. Fiziki* **91**, 968 (2021, in Russian).

[29]R. Zhang, B. Jiang and W. Cao, Elastic, piezoelectric, and dielectric properties of multidomain 0.67Pb($Mg_{1/3}Nb_{2/3}$)O_3–0.33$PbTiO_3$ single crystals, *J. Appl. Phys*. **90**, 3471 (2001).